Growth of Highly Epitaxial YBa2Cu3O7−δ Films from a Simple Propionate-Based Solution

ARTICLE *in* INORGANIC CHEMISTRY · OCTOBER 2015

Impact Factor: 4.76 · DOI: 10.1021/acs.inorgchem.5b01486

Inorganic Chemistry

Article

pubs.acs.org/IC

Growth of Highly Epitaxial $YBa_2Cu_3O_{7-\delta}$ Films from a Simple Propionate-Based Solution

Yue Zhao,*[,†,‡] Pol Torres,[†,§] Xiao Tang,[∥] Poul Norby,[†] and Jean-Claude Grivel[†]

[†]Department of Energy Conversion and Storage, Technical University of Denmark, Frederiksborgvej 399, Roskilde 4000, Denmark

[‡]Department of Electrical Engineering, Shanghai JiaoTong University, 200240 Shanghai, People's Republic of China

[§]Departament de Física, Universit at Autònoma de Barcelona, Bellaterra 08193, Catalonia, Spain

[∥]Institute of Physical Chemistry, University of Hamburg, Grindelallee 117, Hamburg 20146, Germany

ABSTRACT: Intensive investigations have been conducted to develop epitaxial oxide thin films with superior electromagnetic performance by low-cost chemical solution deposition routes. In this paper, a novel propionate-based precursor solution without involving any other additive was proposed and employed to grow superconducting $YBa_2Cu_3O_{7-\delta}$ (YBCO) films on $LaAlO_3$ (LAO) single crystals. The precursor solutions are stable with a long shelf life of up to several months. Since the primary compositions are propionates after evaporating the solvent, the toxic reagents and evolved gases during solution synthesis and heat treatment can be eliminated completely. In this process, rapid pyrolysis and high conversation rate can also be achieved during growth of YBCO films in comparison with the conventional trifluoroacetate metal organic deposition routes. Remarkably, a 210 nm YBCO film exhibits high superconducting performance with a J_c value of 3.7 MA/cm^2 at 77 K, self-field. Nucleation and growth behaviors in the chemical solution process have also been studied. It is revealed that the amount of liquid phase (Ba−Cu−O) is sufficient through the entire thickness within a very short time at high growth temperatures, which results in pronounced densification and fast conversion of the YBCO phase.

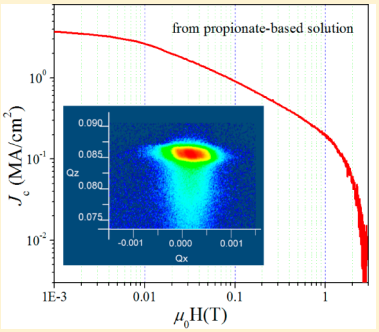

1. INTRODUCTION

Chemical solution deposition routes have attracted more and more attention, to develop functional oxide thin films with unique and superior electromagnetic performance.[1−3] Both the compositions and the microstructures of the oxide films can be modulated through precursor solutions, substrate materials, and heat treatment procedures. As an example, chemical solution deposition (CSD) techniques have been successfully employed in fabrication of $YBa_2Cu_3O_{7-\delta}$ (YBCO) on the basis of the second-generation high-temperature superconductors (so-called "coated conductors", CCs),[4,5] which have a great potential for applications in cables, electronics, etc. These techniques not only offer the possibility of achieving the price targets by reducing the production cost but also allow increasing the superconducting performance either by controlling the solution chemistry or by further optimizing nucleation and growth behaviors during the amorphous−crystalline transition.

The solutions for synthesis of YBCO films are diverse. Depending on the presence of fluorine in the precursors, CSD routes can be categorized into trifluoroacetate metal organic deposition (all TFA-MOD or low TFA-MOD) and fluorine-free (FF)-solution routes. The essential difference between these two routes from the point of view of reaction mechanism is associated with the key intermediate phases after pyrolysis. For example, in the conventional TFA-MOD route, BaF_2 plays an important role in order to avoid the formation of $BaCO_3$, which was initially believed to be the origin of the weak-link behavior in YBCO films grown by FF-solution routes.[6,7] With the advancement of further understanding of the growth mechanisms, FF-solution routes have recently achieved high superconducting performance in YBCO films and have been drawn back into focus.[8−10]

In contrast to the conventional TFA routes, the FF-solution routes offer the possibility of fast pyrolysis and much higher growth rate. For the synthesis of the FF precursors, the starting reagents vary from metal−organic compounds with complex structure (such as acetylacetonates,[11] naphthenates,[12] and trimethyl acetates[13]) to simple metal salts (nitrates,[14,15] acetates,[16−18] and propionates[19]). In order to obtain homogeneous elemental distribution at the atomic level in the precursors, chelating agents and/or rheology modifiers are necessarily required either to form a 3D network comprising all/most of the cations or to increase the solubility of the reagents. It is therefore crucial to regulate the pH value for preventing segregation and/or precipitation in most of the cases. Such processes make the solution chemistry considerably pH sensitive because of the relatively narrow window of pH value for stabilizing the precursor solutions.[17,19] Additionally, the chelating agents or rheology modifiers commonly used are ammonia or its derivatives (e.g., triethanolamine).[10,13,17] Therefore, the pollution caused by the byproducts during solution synthesis and the evolved gases (most likely toxic: i.e.,

Received: July 3, 2015

DOI: 10.1021/acs.inorgchem.5b01486
Inorg. Chem. XXXX, XXX, XXX−XXX

nitrogen oxides) during pyrolysis has to be taken into consideration in environmentally friendly processes.

In this paper, for the first time, we propose a simple FF solution based on propionate salts without any nitrogen-containing chelating agents, and epitaxial YBCO films with high J_c values were obtained on $LaAlO_3$ (LAO) single crystals. The precursor and the fully reacted YBCO films were characterized and investigated. In addition, a comparative study between the films grown from LF TFA and FF solutions were also carried out in terms of the structural characteristics and the superconducting performance. The growth mechanism of YBCO films made by such novel FF solutions is also discussed on the basis of the comprehensive microstructure characterizations of partially reacted specimens.

2. EXPERIMENTAL PROCEDURES

2.1. Solution Synthesis. The FF-YBCO precursor solutions were synthesized by mixing stoichiometric amounts (1:2:3) of Y, Ba, and Cu acetates, i.e., $Y(CH_3COO)_3{\cdot}xH_2O$ (Purity 99.9%, Sigma-Aldrich), $Ba(CH_3COO)_2$ (Purity 99%, Alfa-Aesar), and $Cu(CH_3COO)_2{\cdot}H_2O$ (purity 98%, Alfa-Aesar), into propionic acid (Purity 99%, Alfa-Aesar). After the mixture was stirred at 80 °C for about 1 h on a hot plate, all of the starting reagents were dissolved, and dark blue solutions without any precipitation were obtained. The concentration of the precursor solutions was simply adjusted in the range from 1.7 to 1.5 M by adding propionic acid.

2.2. Film Growth. The precursor solutions were deposited onto 5 mm × 5 mm (001) LAO single-crystal substrates (CrysTec GmbH) by spin coating (rotation speed from 3000 to 6000 rpm). A typical three-step heat treatment process including pyrolysis, sintering, and oxygenation was performed in an atmosphere-controlled tubular furnace. First, the coated films were directly inserted into the furnace preheated at about 100 °C in order to avoid unnecessary water absorption under ambient conditions and heated to 470 °C with a ramp rate of 10 K/min in a humid oxygen flow with a dew point of room temperature. Second, the sintering process was performed at about 810 °C with a heating ramp of 20 K/min for 1 or 2 h depending on the film thickness under flowing dry forming gas (300−500 ppm of O_2 in N_2). Finally, the samples were oxygenated at 450 °C for 3 h.

2.3. Characterization. Fourier transform infrared (FT-IR) spectra were obtained with a Bruker Tensor 27 spectrometer at room temperature on the precursor solution coated and dried on a piece of quartz plate at 40 °C. The phase, global texture, and reciprocal spacing maps of the films were collected by means of high-resolution XRD with Cu Kα radiation in a four-circle diffractometer (Rigaku, Smartlab). Film morphology and film thickness were observed in a SEM instrument (Zeiss Supra 35) equipped with an in-lens detector. The local phase on the film surface was determined by analyzing the Kikuchi pattern recorded by an electron backscattering diffraction detector. Normal operating conditions (electron energy of 15 kV in high-current mode) and a commercial software package (Channel 5) were used to acquire and analyze the patterns, respectively. An X-ray energy dispersive spectrometer (EDS) implemented in the Zeiss Supra 35 instrument was used for elemental distribution analysis, and the software NSS (Thermo Fischer Scientific Inc.) was used to analyze the data. The critical current densities, J_c, were calculated on the basis of the Bean model using the opening of the hysteresis loops obtained by a vibrating sample magnetometer (VSM) under magnetic fields applied perpendicular to the plane of the films.

3. RESULTS AND DISCUSSION

3.1. Investigation of Precursor Solution and Pyrolyzed Films. First, the precursor coated and dried on a quartz plate was investigated by FT-IR, as shown in Figure 1. Peaks at the wavenumbers 1532, 1416, and 1286 cm^{-1} are attributed to the COO^- symmetric and asymmetric stretching and symmetric CH_2^-vibrations, respectively. By calculating the

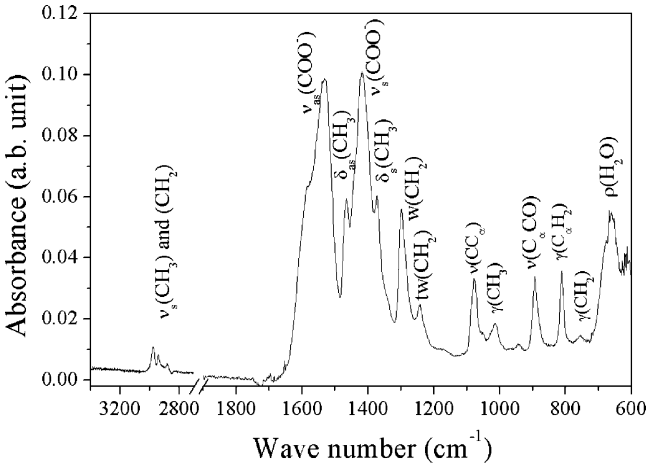

Figure 1. FTIR spectrum of the dried precursor.

difference between the two COO^- frequencies, $\Delta\nu = \nu_{as} - \nu_s$, one could in principle acquire information about the coordination type of the metal ions by the carboxylate ion: chelating bidentate or bridging tridentate.[20] In our case the value of $\Delta\nu$ = 115 cm^{-1} indicates a mixed coordination. In comparison with the FT-IR spectra of individual propionates,[21−23] we noticed broadening for $\nu_{as}(COO^-)$ and $\nu_s(COO^-)$ resulting from the peak overlapping of the multiple compositions in one precursor. Otherwise, the features in the FT-IR spectrum are similar to those of other individual propionates. By studying the decomposition behaviors of individual Y, Ba, and Cu propionates by XRD, FT-IR and thermal analysis, we found that the final decomposition products show that the total relative weight losses after final decomposition are in very good agreement with the theoretical losses calculated for the conversion of respective propionates to the corresponding products.[24] These results further confirm that the acetates are mainly converted to the propionates. Additionally, a study of the shelf life of this precursor solution shows that there is no precipitation after storage for several months, ensuring a high reproducibility of YBCO film deposition. Since the gases evolved during pyrolysis of the propionates in the precursors are mainly symmetrical ketones[21,23,25] with low toxicity (basically at the same hazard level as alcohol, according to the *Materials Safety Data Sheet* from www.sciencelab.com), this precursor solution offers great advantages in terms of environmental safety for both solution synthesis and heat treatment processes. Second, the film morphology after pyrolysis was also investigated by SEM, revealing a homogeneous microstructure without any feature at low magnification, as shown in Figure 2. The absence of defects implies that the stress caused by the chemical reactions is released smoothly with relatively high ramping speed (10 K/min) for the pyrolysis and is below the level which could generate buckling and wrinkles, at least under these conditions. However, the coexistence of two types of particles with significant size differences is discerned in the high-magnification image. This is probably related to different decomposition behaviors of the propionates (e.g., the temperature of combusting the primary organic groups is lower in copper(II) propionate than in yttrium(III) and barium(II) propionates[25,26]). In fact, similar features with copper oxide segregation on the film surface are commonly observed in the pyrolyzed films regardless of the presence of fluorine in the

DOI: 10.1021/acs.inorgchem.5b01486
Inorg. Chem. XXXX, XXX, XXX−XXX

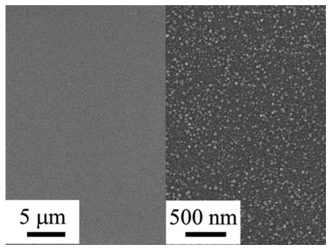

Figure 2. SEM images of a representative film after pyrolysis (results in a thickness of about 450 nm after the full process). Left and right images correspond to low (×2.77 K) and high (×100 K) magnifications, respectively. Note that thinner films exhibit a similar morphology, while thicker films made by a monocoating procedure have microcracks.

precursor. Additionally, the primary intermediate phases, including $BaCO_3$, CuO, and traces of Y_2O_3 are detected by XRD in the pyrolyzed film, as shown in Figure 3. This is similar

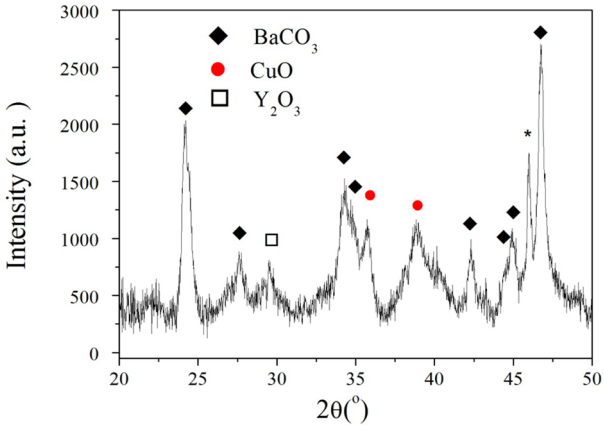

Figure 3. XRD scan on a YBCO film after pyrolysis. Note that, in order to enhance the signal intensity from the intermediate phases, the sample was prepared by repeating the coating and pyrolysis five times.

to the other pyrolyzed films derived from various FF solutions, implying that $BaCO_3$ formation is energetically favorable in most cases unless a large enough amount of fluorine is present.[27]

3.2. Structure Characterization and Superconducting Performance on YBCO Films Derived from Fluorine-Free Solution. The YBCO films with two thicknesses of 210 and 450 nm were grown under the aforementioned optimized conditions. The superconducting properties of the films are also compared with those of a YBCO film prepared by using a low TFA-MOD route published previously.[28] ac susceptibility measurements show that the superconducting transition temperatures (T_c(onset)) for all of the films are around 90 K with a transition width of about 2 K. The $J_c(B)$ dependence at 77 K on a log−log scale of all the films shows similar behaviors, as plotted in Figure 4. Remarkably, a J_c value of 3.7 MA/cm^2 is achieved in the 210 nm thick FF YBCO film measured at 77 K self-field which is quite comparable with that on the 220 nm thick film grown by the low TFA-MOD route. The J_c value at 77 K self-field not surprisingly decreases to 2.2 MA/cm^2 on the 450 nm thick FF-YBCO film (the maximum thickness that could be achieved by monocoating using this precursor). Suppression of J_c values with thickness is widely observed regardless of deposition techniques.[29,30] A decrease in density

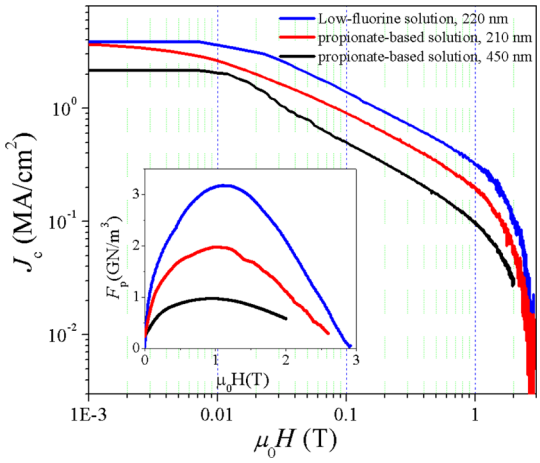

Figure 4. Double-logarithmic plots of J_c vs magnetic field $\mu_0 H$ measured at 77 K for both the FF-YBCO films and the reference sample deposited by the conventional low TFA-MOD route. Inset: flux pinning forces of all three films at 77 K.

of vortex pinning centers could be the main explanation in this case. As can be seen in the pinning force (F_p) calculated from $J_c \times B$ at 77 K on all three samples (Figure 4. inset), even for the 210 nm thick FF-YBCO film, the maximum pinning force is 2.0 GN/m^3, about 30% lower than that in the low TFA-MOD YBCO film. F_p is known as the force that immobilizes magnetic flux lines by preferably nonsuperconducting defects. It is therefore supposed that there are fewer such defects acting as pinning centers in FF-YBCO films due to the different growth mechanisms.

To shed the light on the difference in superconducting properties, detailed microstructure characterizations were performed on the YBCO films with comparable thicknesses but obtained from FF and TFA precursors. As seen in Figure 5a, the XRD $\theta-2\theta$ scans on both YBCO films show predominantly c axis growth, as evidenced by strong (00l) peaks, the absence of (200) peaks, and negligible (013)/(103) peaks. The lengths of the c axes of the FF- and TFA-YBCO films are very similar, around 11.67 Å, close to that for powders and single crystals. In addition, we notice an obvious asymmetric peak broadening of (001), (002), and (004), more visible in the low TFA-YBCO film. These are typical features of $YBa_2Cu_4O_x$ formation (124-type intergrowths).[31] The 124-phase well oriented along the ab plane (confirmed from the reciprocal spacing maps of the YBCO (001) reflection in Figure 5b) is associated with the barium cuprite (Cu^{1+}) particles incorporated in laminar structures of the YBCO films[32] grown by an ex situ route (for both TFA and FF routes). As a planar defect parallel to the ab planes, the 124-phase definitely enhances the $J_c(H)$ value when $H \| ab$. It is worth pointing out that partial dislocations associated with the formation of 124-type intergrowths might also act as point pinning centers when the low magnetic field is away from the ab planes.[33]According to a detailed XRD $\theta-2\theta$ and texture analysis, we could also determine that the strains along the c axis are 0.21% and 0.08% for TFA-and FF-YBCO films, respectively, confirming the greater extent of disorder in the FTA-MOD YBCO film. The full width at half maximum (FWHM) values of the YBCO (005) rocking curves for these two films are 0.8 and 0.15°, respectively, while the splitting of the peaks in the YBCO (103) ϕ scan is separated by about 0.9° with respect to each other in the FF-YBCO film; this is absent

DOI: 10.1021/acs.inorgchem.5b01486
Inorg. Chem. XXXX, XXX, XXX−XXX

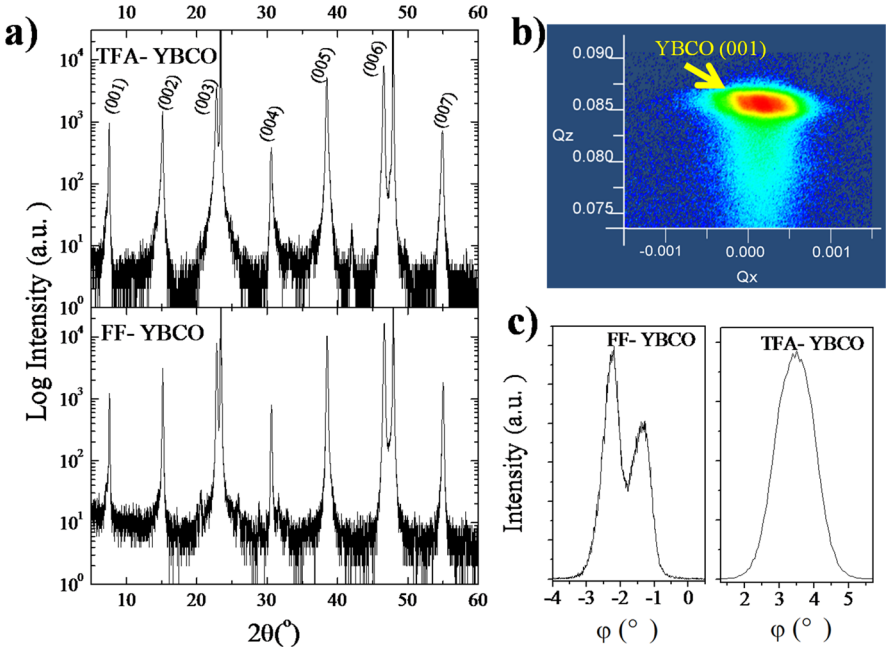

Figure 5. X-ray diffraction analysis of the FF- and TFA-YBCO films: (a) θ–2θ scans, where the unmarked reflections are from the substrate; (b) reciprocal spacing maps of the YBCO (001) reflection on the 210 nm thick FF-YBCO film, with log-scaled intensity; (c) YBCO (103) ϕ scans for the FF-YBCO (left) and TFA-YBCO (right) films.

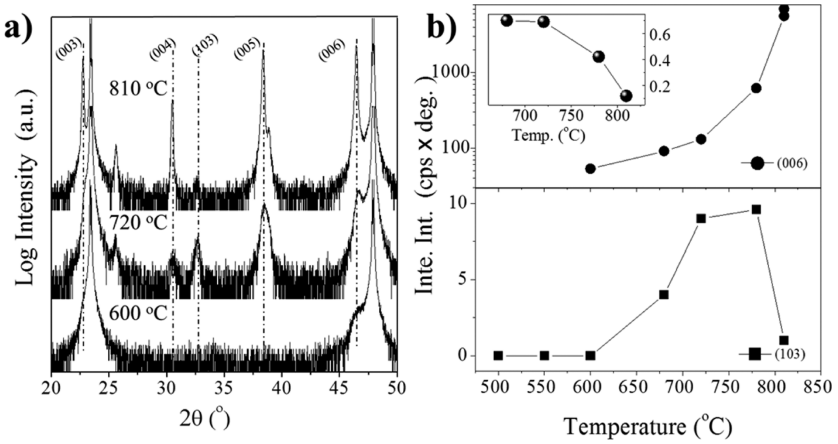

Figure 6. X-ray diffraction analysis on the specimens quenched at different temperatures: (a) θ–2θ scans; (b) integrated intensities of the YBCO (006) (upper) and (103) (lower) peaks as a function of temperature. The inset in the upper panel shows the evolution of the FWHM values of YBCO (005) rocking curves.

in TFA-YBCO film. This is clearly due to the twinning in the *ab* plane, being indicative of a superior quality of crystal structure in the FF-YBCO film.

All of these structural characteristics indeed suggest a greater amount of defects in the TFA-YBCO film, which are the origin of the higher F_p values in the TFA-YBCO film. It is therefore necessary to induce artificial pinning centers in the YBCO matrix to further improve the superconducting performance for both thin and thick FF-YBCO films in the future.

3.3. Discussion of Nucleation and Growth Behaviors in Fluorine-Free YBCO Films. The nucleation and growth behaviors were studied by examining specimens quenched from different temperatures. First, the XRD θ–2θ scans were carried out in order to get a first insight into the phase evolution during sintering. As shown in Figure 6a, the broad YBCO (006) peak is discerned as early as 600 °C. At elevated temperatures, weak YBCO (103) is also detected, being indicative of homogeneous nucleation. Both the textured and polycrystalline grains grow simultaneously until 780 °C (as plotted in Figure 6b). Two peaks at 25.5 and 38.7°, which are assigned as intermediate phase $Ba_2Cu_3O_{5.9}$ (ICCD 46-0269), were also observed in a broad temperature range from 680 to 810 °C. This intermediate phase is undetectable when the dwell time is prolonged to 30 min. The integrated intensity of the YBCO (006) reflection increases dramatically, nearly 1 order of magnitude, from 780 to 810 °C, and the YBCO (103) peak intensity becomes negligible. Meanwhile, the FWHM values of the YBCO (005) rocking curves decrease to 0.1° at 810 °C (plotted in the inset of Figure 6b, upper panel). Considering the high ramping rate, such pronounced changes take place within 2 min, indicating a fast YBCO grain growth as well as structure rearrangement behavior.

Accordingly, SEM combined with EDS analysis was carried out on several representative quenched specimens. The first

DOI: 10.1021/acs.inorgchem.5b01486
Inorg. Chem. XXXX, XXX, XXX–XXX

SEM image was acquired from the 600 °C quenched film. Even though the YBCO phase already forms at this low temperature, a striking morphological feature is hardly seen on the surface. Small amounts of pinholes are present (as denoted by arrows in Figure 7a), probably due to the release of CO_2 gas during the reaction between $BaCO_3$ and CuO. We suppose that this temperature is close to the starting point of formation of the liquid phase, from which the textured YBCO crystals mainly nucleate at the interface.

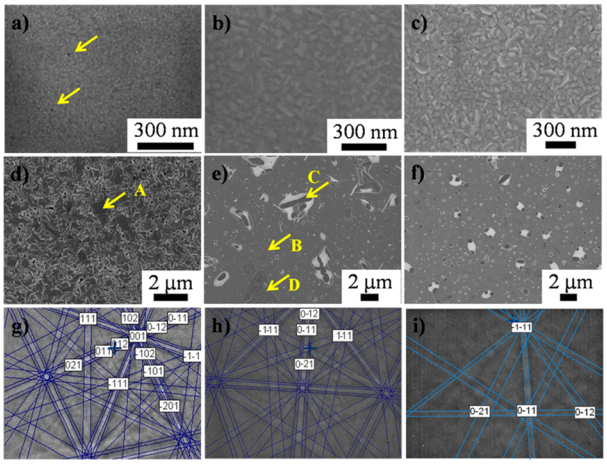

Figure 7. SEM images on the specimens quenched at different temperatures: (a–e) quenching from 600, 680, 720, 780, and 810 °C, respectively, without any dwell time; (f) quenching from 810 °C after dwelling for 30 min. Representative Kikuchi patterns with phase indexation acquired (g) on a large platelike grain in the 780 °C quenched specimen, (h) on a dense and flat region, and (i) on a large Y-rich particle.

With elevation of the sintering temperatures to 780 °C (Figure 7b–d), the grains coarsen progressively, and no element segregation is found by EDS mapping. A minority of the grains with small grain size (GS) remain spherical, while the others with lateral GS up to the micrometer level exhibit an irregular morphology. The coexistence of two types of grains and prominent nonuniform grain size distribution is indicative of a process governed by the solution–reprecipitation mechanism.[34] Pores with irregular shape are present at grain boundaries (Figure 7d), implying a serious shrinkage resulting from the reactions. However, it seems that the capillary force is not strong enough to densify the microstructure, due to a limited amount of liquid phase. By checking local phases and their distribution using the EBSD technique, we found that the large platelike grains (e.g., that denoted by arrow A in Figure 7d) corresponds to the YBCO phase very well (Figure 7g) . Further EBSD mapping reveals that YBCO grains cover at least 45% of the surface of the 780 °C quenched specimen but with completely random orientation. When this was combined with the aforementioned results, it was confirmed that the weak YBCO (103) reflection detected in the XRD scan is indeed attributable to bulk nucleation in the film body, which is however overwhelmed by dominant epitaxial growth close to the interface, as evidenced by the strong YBCO (00*l*) peaks.

The most dramatic changes in morphology occur at 810 °C, in agreement with the XRD results. Almost all of the nanosized grains disappear at 810 °C (Figure 7e). Instead, a rather dense microstructure with a smooth surface is present on most of the film surface. Interestingly, in combination with an elemental distribution mapping analysis by EDS (Figure 8), we also noticed different features corresponding to evolution of YBCO

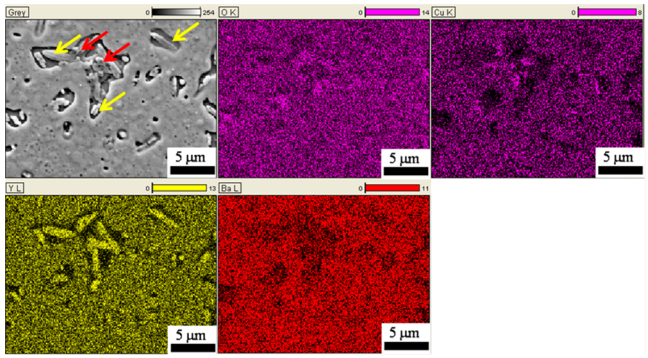

Figure 8. EDS mapping images for O, Cu, Y, and Ba presented in an autoscaled color scale. The corresponding SEM image is also included. It can be seen that Y-rich inclusions (denoted by yellow arrows, for example) up to about 5 μm are present in Ba- and Cu-poor areas, while there are small amounts of Cu-rich particles (denoted by red arrows, for example) with much smaller grain size.

formation at two stages. That is, (i) a smooth microstructure with meandering grain boundaries (denoted by arrow B) represents nearly fully reacted YBCO with good texture (confirmed by Kikuchi patterns matching with the *c* axis YBCO phase representatively shown in Figure 7h) and (ii) large Y_2O_3 particles isolated from or partially connected with melted structure (denoted by arrow C, for example) represent unreacted regions. The region denoted by arrow D shows a typical morphology representing the reaction stage between. The features for the partially reacted regions are apparently due to the surface tension, which keeps the liquid phase together, leading to meandering boundaries, and leaves secondary phase particles behind. After the dwell time is prolonged at 810 °C (Figure 7f), the reaction between the liquid phase and the secondary phase particles further proceeds until all of the isolated particles are merged into the liquid phase. Meanwhile, the amount of other defects and the uncovered regions are significantly reduced.

Such morphology changes are closely related to the growth mechanism of YBCO films derived from FF-MOD solutions. Investigations of the chemical reaction path of YBCO powder/bulk made from FF precursors suggest that YBCO formation is basically governed by three steps from the intermediate phases after pyrolysis ($BaCO_3$, CuO, and Y_2O_3).[35−37]

To the best of our knowledge, there are few reports in the literature on the evolution of FF-MOD derived YBCO films with high performance. In the studies of YBCO powder formation, strong evidence supports the existence of the liquid phase and finial reaction between the liquid phase and the secondary phase particles.[38,39] In this work, we also found significant differences in comparison with the conversion of the YBCO in powder samples. First, the textured YBCO crystalline nucleating at the interface appears below 600 °C, while there is no clear proof of the presence of the liquid phase on the surface. This suggests that the proposed reactions could be triggered at much lower temperature probably due to the small Gibbs free energy required for heterogeneous nucleation. Second, prior to the presence of the enhanced liquid phase observed at 810 °C, the textured and polycrystalline YBCO grains grow simultaneously. Apparently, oriented YBCO grains

DOI: 10.1021/acs.inorgchem.5b01486
Inorg. Chem. XXXX, XXX, XXX−XXX

have a significant preferential growth advantage at higher temperature, and such an advantage becomes more pronounced in the presence of a large amount of liquid phase at the target temperature of 810 °C. Third, at 810 °C a large extent of the liquid phase is present, which allows for mass transport to occur on a micrometer scale laterally across the films. As a result, YBCO films with dense and smooth structure exhibit rather fast growth behavior at this stage and are characterized by a striking overgrowth feature.

It is well accepted that a so-called "transient liquid phase"[40−42] plays an important role during the YBCO conversion in the ex situ BaF_2 processes for both physical vapor deposition and MOD techniques. In this scenario, YBCO crystals nucleate at the substrate interface and mainly grow into the precursor in a layer by layer manner due to the limited amount of the liquid phase. As a result, surface morphologies commonly feature small porosity or granular grains. However, our study of the FF process reveals that the amount of liquid phase at high sintering temperature is enough through the entire thickness spreading over several micrometer scales, leading to a dense and smooth surface without distinguishable grain boundaries. Strikingly, YBCO formation is mainly governed by such a two-dimensional layer-extension mode.

4. CONCLUSION

In this paper, we have proposed a novel FF-precursor solution, which only uses propionic acid as solvent, without any other additive. The precursor solutions are environmentally friendly and are stable with a long shelf life of up to several months. Intermediate phases ($BaCO_3$, CuO, and Y_2O_3) are similar to those in other fluorine-free processes. Remarkably, two 210 and 450 nm thick YBCO films exhibit high superconducting performance with J_c values of 3.7 and 2.1 MA/cm^2 at 77 K self-field, respectively. Due to the superior crystal structure in the FF-YBCO film, lower pinning force densities are found in comparison with a typical YBCO film with similar thickness but grown by the conventional low TFA-MOD route. We further investigated the nucleation and growth behaviors in the FF-solution process using the films quenched at various growth temperatures, which differ from those previously studied in the bulk or powder specimens. It is found that YBCO heterogeneous nucleation occurs at much lower temperature, whereas a sufficient amount of the liquid phase through the entire thickness is present at high temperatures. The enhanced liquid phase exhibits a great difference in comparison to the traditional TFA processes and results in a pronounced microstructure evolution and rapid conversion of the YBCO phase.

AUTHOR INFORMATION

Corresponding Author

*E-mail for Y.Z.: yuezhao@sjtu.edu.cn.

Notes

The authors declare no competing financial interest.

REFERENCES

(1) Llordes, A.; Palau, A.; Gazquez, J.; et al. *Nat. Mater.* **2012**, *11*, 329−336.
(2) Liu, G.; Liu, A.; Zhu, H.; et al. *Adv. Funct. Mater.* **2015**, *25*, 2564−2572.
(3) Fei, L.; Naeemi, M.; Zou, G.; et al. *Chem. rec.* **2013**, *13*, 85−101.
(4) Rupich, M. W.; Li, X.; Thieme, C.; et al. *Supercond. Sci. Technol.* **2010**, *23*, 014015.
(5) Sheehan, C.; Jung, Y.; Holesinger, T.; et al. *Appl. Phys. Lett.* **2011**, *98*, 071907.
(6) Araki, T.; Yamagiwa, K.; Hirabayashi, I.; Suzuki, K.; et al. *Supercond. Sci. Technol.* **2001**, *14*, L21−24.
(7) Parmigiani, F.; Chiarello, G.; Ripamonti, N. *Phys. Rev. B: Condens. Matter Mater. Phys.* **1987**, *36*, 7148−7150.
(8) Yamasaki, H.; Ohki, K.; Yamaguchi, I.; et al. *Supercond. Sci. Technol.* **2010**, *23*, 105004.
(9) Lei, L.; Zhao, G.; Bai, Y.; et al. *J. Supercond. Novel Magn.* **2014**, *27*, 23−26.
(10) Tang, X.; Zhao, Y.; Wu, W.; et al. *J. Eur. Ceram. Soc.* **2015**, *35*, 1761−1769.
(11) Matsui, H.; Tsukada, K.; Tsuchiya, T.; et al. *Phys. C* **2011**, *471*, 960−962.
(12) Ma, X. L.; Hirayama, T.; Yamagiwa, K.; et al. *Phys. C* **1998**, *306*, 245−252.
(13) Xu, Y.; Goyal, A.; Rutter, N. A.; et al. *J. Mater. Res.* **2003**, *18*, 677−681.
(14) Apetrii, C.; Schlorb, H.; Falter, M.; et al. *IEEE Trans. Appl. Supercond.* **2005**, *15*, 2642−2644.
(15) Patta, Y. R.; Wesolowski, D. E.; Cima, M. J. *Phys. C* **2009**, *469*, 129−134.
(16) Wang, W. T.; Pu, M. H.; Wang, W.; et al. *J. Supercond. Novel Magn.* **2010**, *23*, 989−993.
(17) Schoofs, B.; Cloet, V.; Vermeir, P.; et al. *Supercond. Sci. Technol.* **2006**, *19*, 1178.
(18) Tang, X.; Zhao, Y.; Grivel, J.-C. *Ceram. Int.* **2013**, *39*, 7735−7741.
(19) Tang, X.; He, D.; Zhao, Y.; Grivel, J.-C. *IEEE Trans. Appl. Supercond.* **2014**, *24*, 74.
(20) Deacon, G. B.; Phillips, R. J. *Coord. Chem. Rev.* **1980**, *33*, 227−250.
(21) Grivel, J.-C. *J. Anal. Appl. Pyrolysis* **2013**, *101*, 185−92.
(22) http://webbook.nist.gov/cgi/cbook.cgi?ID=B6000148&Mask=80.
(23) Nasui, M.; Mos, R. B.; Petrisor, T., Jr; et al. *J. Anal. Appl. Pyrolysis* **2011**, *92*, 439−444.
(24) Torres, P. Studies on thermal decomposition of Ba and Cu carboxylates and application to the synthesis of $ReBa_2Cu_3O_{7-x}$ superconductors (RE = rare earth); Master's thesis, 2014.
(25) Nasui, M.; Petrisor, T., Jr; Mos, R. B.; et al. *J. Anal. Appl. Pyrolysis* **2014**, *106*, 92−98.
(26) Mos, R. B.; Nasui, M.; Petrisor, T., Jr; et al. *J. Anal. Appl. Pyrolysis* **2011**, *92*, 445−449.
(27) Wu, W.; Feng, F.; Zhao, Y.; et al. *Supercond. Sci. Technol.* **2007**, *19*, 055006.
(28) Zhao, Y.; Wu, W.; Tang, X.; et al. *CrystEngComm* **2014**, *16*, 4369−4372.
(29) Kim, S. I.; Gurevich, A.; Song, X.; et al. *Supercond. Sci. Technol.* **2006**, *19*, 968−979.
(30) Develos-Bagarinao, K.; Yamasaki, H.; Nie, J. C.; et al. *Supercond. Sci. Technol.* **2005**, *18*, 667−674.
(31) Specht, E. D.; goyal, A.; Li, J.; et al. *Appl. Phys. Lett.* **2006**, *89*, 162510.
(32) Zhang, W.; Huang, Y.; Li, X.; et al. *IEEE Trans. Appl. Supercond.* **2007**, *17*, 3347−3350.
(33) Gutierrez, J.; Maiorov, B.; Puig, T.; et al. *Supercond. Sci. Technol.* **2009**, *22*, 015022.
(34) Chu, P.; Buchanan, R. C. *J. Mater. Res.* **1994**, *9*, 844−851.
(35) Chu, P.; Buchanan, R. C. *J. Mater. Res.* **1993**, *8*, 2134−2142.
(36) Lay, K. W.; Renlund, G. M. *J. Am. Ceram. Soc.* **1990**, *73*, 1208−1213.
(37) Vermeir, P.; Cardinael, I.; Schaubroeck, J.; et al. *Inorg. Chem.* **2010**, *49*, 4471−4477.
(38) Roth, R. S.; Davis, K. L.; Dennis, J. R. *Adv. Ceram. Mater.* **1987**, *2*, 303−313.
(39) Nakahara, S.; Fisanick, G. J.; Yan, M. F.; van Dover, R. B.; Boone, T. *J. Cryst. Growth* **1987**, *85*, 639−651.

DOI: 10.1021/acs.inorgchem.5b01486
Inorg. Chem. XXXX, XXX, XXX−XXX

(40) Wu, L.; Zhu, Y.; Solovyov, V. F.; et al. *J. Mater. Res.* **2001**, *16*, 2869−2884.
(41) Holesinger, T. G.; Arendt, P. N.; Feenstra, R.; et al. *J. Mater. Res.* **2005**, *20*, 1216−1233.
(42) Gazquez, J.; Sandiumenge, F.; Coll, M.; et al. *Chem. Mater.* **2006**, *18*, 6211−6219.

DOI: 10.1021/acs.inorgchem.5b01486
Inorg. Chem. XXXX, XXX, XXX−XXX